

## Modulating Surface Redox Reactions and Solvated Electron Emission on Boron-Doped Diamond by (Photo)electrochemistry

Arsène Chemin<sup>1,2,\*</sup>, Louis Godeffroy<sup>1</sup>, Marin Rusu<sup>1</sup>, Michael Drisch<sup>3</sup>, Maik Finze<sup>3</sup>, Peter Knittel<sup>4</sup>, Anke Krueger<sup>5</sup>, and Tristan Petit<sup>1</sup>


<sup>1</sup>Nanoscale Solid-Liquid Interfaces, *Helmholtz-Zentrum Berlin für Materialien und Energie GmbH, Albert-Einstein Straße 15, 12489 Berlin, Germany*

<sup>2</sup>Department of Physics, *Institut Lumière Matière, Université Claude Bernard Lyon 1, CNRS, UMR5306, F-69100 Villeurbanne, France*

<sup>3</sup>Institute of Inorganic Chemistry, Institute for Sustainable Chemistry & Catalysis with Boron (ICB), *Julius-Maximilians-Universität Würzburg, Am Hubland, 97074 Würzburg, Germany*

<sup>4</sup>Department Quantum Technologies, *Fraunhofer-Institut für Angewandte Festkörperphysik, Tullastraße 72, 79108 Freiburg, Germany*

<sup>5</sup>Institute for Organic Chemistry, *University of Stuttgart, Pfaffenwaldring 55, 70569 Stuttgart, Germany*

 (Received 17 March 2025; revised 6 June 2025; accepted 1 August 2025; published 28 August 2025)

The interplay between photochemical and electrochemical reactions fundamentally influences charge transfer processes at solid-liquid interfaces. Nevertheless, chemical processes at semiconductor surfaces triggered by light excitation under an applied potential remain poorly explored. This work deciphers the synergistic effect of potential and light excitation on boron-doped diamond electrodes in producing either surface redox reactions or emission of solvated electrons in water. The effect of diamond surface termination on electron affinity, band bending, and charge extraction is identified in a photoelectrochemical cell. While photocurrent is observed for excitation as low as 3.5 eV, we show that it is induced mostly by surface redox reactions, whereas solvated electrons are detected only for excitation above the band gap (5.47 eV). Solvated electrons are generated irrespective of band bending, which affects only the emission yield. Depending on the surface band bending, photoreduction of the hydroxylated surface groups and photooxidation of the C—H surface groups can be induced by direct photoexcitation in the range of 4.2–4.8 eV. The surface of the diamond can be electrochemically reduced when the Fermi level of the oxidized surface decreases below the H<sup>+</sup>/H<sub>2</sub> redox potential. On the other hand, the hydrogenated surface oxidizes spontaneously for potentials at which the Fermi level drops below the occupied C—H surface states, depending on both the pH and the electron affinity of the surface. This work provides insights into (photo)redox processes on diamond materials, which may find applications in photoelectrochemical solar fuel generation or energy storage.

DOI: [10.1103/zhcb-13pn](https://doi.org/10.1103/zhcb-13pn)

### I. INTRODUCTION

As an alternative to fossil fuels, chemical products derived from renewable and abundant solar energy, also known as “solar fuels,” are attracting increasing attention. The simplest way to produce solar fuels such as H<sub>2</sub>, C<sub>2</sub>H<sub>2</sub>, or CH<sub>3</sub>OH is by coupling standard photovoltaic cells to electrolyzers. Taking advantage of the maturity of these two technologies, this approach enabled a fast development of solar fuels, which are now close

to reaching the market. However, to prevent additional efficiency losses due to external coupling, direct photoelectrochemical (PEC) conversion would be preferable [1]. PEC conversion uses wide band gap (greater than 1.5 eV) semiconducting materials (e.g., TiO<sub>2</sub>, Cu<sub>2</sub>O, Fe<sub>2</sub>O<sub>3</sub>) as light absorbers [2]. For large enough band gaps, the photon energy can compensate for the overpotential needed for the electrochemical reaction, and the reduced working potential helps save electrical power as well as increase selectivity. PEC conversion experienced a significant revival following the use of high surface area nanostructured electrodes inspired by the design of dye-sensitized colloidal TiO<sub>2</sub> films by O’Regan and Grätzel [3]. Since then, a variety of materials and strategies have been explored to increase the efficiency of PEC conversion, yet numerous challenges persist.

TiO<sub>2</sub> remains the most used semiconductor in photocatalysis because of its low cost, chemical stability, and

\*Contact author: [arsene.chemin@univ-lyon1.fr](mailto:arsene.chemin@univ-lyon1.fr)

Published by the American Physical Society under the terms of the [Creative Commons Attribution 4.0 International](https://creativecommons.org/licenses/by/4.0/) license. Further distribution of this work must maintain attribution to the author(s) and the published article’s title, journal citation, and DOI.

high oxidative potential. However, the recombination of electron-hole pairs hinders its activity under visible irradiation [4].  $\text{Cu}_2\text{O}$ , otherwise more effective, degrades very quickly due to surface state poisoning, and recent studies have focused on understanding and mitigating this rapid degradation [5]. Hematite ( $\alpha\text{-Fe}_2\text{O}_3$ ) has also been extensively studied as a photoanode material due to its record-high theoretical photocurrent (PC) for water oxidation (based on its relatively narrow band gap of 1.9–2.2 eV) and chemical stability [6]. However, recent studies have demonstrated that only a small fraction of the theoretical photocurrent could ever be reached for hematite photoanodes [7].

Optimizing photoactive materials often involves focusing separately on stability, light absorption, charge transfer, and photoelectroactivity. However, bulk electronic properties and *ex situ* characterizations do not fully explain behaviors under operating conditions. PEC conversion requires stable materials and a good understanding of the interface properties [8] and photoexcitation processes in order to limit charge trapping and electron-hole recombination pathways [9]. Catalytic reactions are highly sensitive to surface chemistry, and the surface termination can significantly modify the band structure of semiconductors, changing the electron affinity and surface band bending. The interplay between these interface properties, along with the applied potential and equilibrium with the electrolyte, significantly influences the overall behavior of the electrode [9,10]. Therefore, a comprehensive analysis that combines interface characterization, photoexcitation, and charge transfer in relation to the applied potential is necessary to grasp the fundamental properties of the electrode and improve its performances.

Because of recent improvements in their production, synthetic boron-doped diamonds (BDDs) are attracting interest with rapidly decreasing fabrication costs and scalable synthesis [11]. BDD is an ideal material for metal-free electrodes for electrochemical reactions under harsh conditions, such as water decontamination, due to its excellent chemical stability, conductivity, and sustainability [12–14]. In the context of direct solar-to-fuel conversion, diamond stands out as a unique photoelectrode material emitting solvated electrons under UV light when doped with boron [15,16], and visible light for detonation nanodiamonds [17], unlocking challenging reactions such as nitrogen [18] and carbon dioxide [19–22] reduction. However, photoelectron yields remain limited, and the coupling of photochemical and electrochemical processes at the diamond/water interface remains poorly understood. Unraveling the mechanisms at play is crucial for finding new strategies to improve solvated electron emission, diamond photoactivity, and selectivity.

Diamond has the specificity of accommodating a broad range of surface terminations (such as H, O, N, and F), which may introduce new electronic states within the band

gap [23,24]. We have recently demonstrated in air that these surface states can be excited in the visible range, despite the inherently wide band gap of diamond [25]. We suggest that this mechanism may be responsible for the photocurrent reported in the literature [26–30], whose origin is still debated. Although this photocurrent has a low yield, it is applicable in specialized fields such as brain implants [30–33] and photoelectrochemistry [34,35]. Distinguishing photocurrent induced by redox reactions involving surface states from the emission of solvated electrons is crucial for assessing the chemical reactivity of diamond in aqueous electrolytes.

In this study, we combine photoelectrochemical and spectroscopic methods to comprehensively analyze the BDD/water interface of nanostructured BDD under illumination and an applied potential, in conditions relevant to producing solar fuels. For this, we consider band diagrams as a framework to explain the macroscopic effects that we observe, not accounting for local phenomena originating from surface inhomogeneity, different crystal facets, doping inhomogeneity, and grain boundaries. Such defects can create localized states, charge carriers, or trapping states, significantly impacting the local behavior of the surface. While they can be of interest for specific applications, they require dedicated studies at the nanoscale, which are beyond the scope of this study. While band diagrams are often simplified models representing the macroscopic or average electronic state of a material, they allow the capture of the overall response of the electrode, enabling an interpretation of charge transfer processes at the diamond/water interface. The characterization of electron affinity, band bending, and charge extraction during photoelectrochemical processes on BDD enhances our understanding of semiconductor/water interfaces.

Dosing of solvated electrons enables the differentiation between light excitation leading to redox reactions at the surface of the diamonds and the emission of solvated electrons. Use of photocurrent cyclic voltammetry (PC-CV) is introduced to provide evidence of electrochemical oxidation and reduction of the surface and spontaneous oxidation in water.

This comprehensive insight into the (photo)electrochemical reactivity of BDD interfaces will allow the design of more-efficient diamond-based photoelectrodes in the future. Beyond diamond, the methods introduced will also have the potential for improving other photoelectrode materials.

## II. RESULTS AND DISCUSSION

### A. Photocurrent spectroscopy

Nanostructured polycrystalline BDDs with needlelike structures of about 100 nm, as shown in the cross-section scanning electron microscopy image presented in Fig. 1(a), were used in this study [19]. These electrodes have bulk

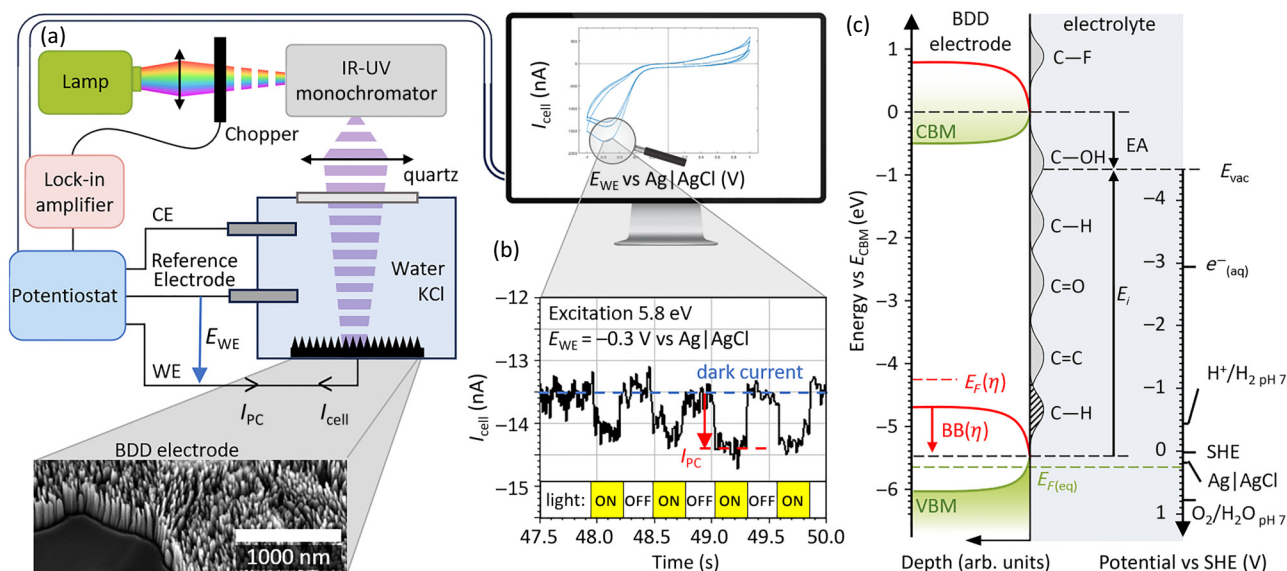


FIG. 1. Photocurrent spectroscopy on nanostructured BDD electrodes. (a) Photoelectrochemical cell and sign conventions, and cross-section scanning electron microscopy view of the nanostructured BDD electrodes used in this study. (b) Cell current  $I_{\text{cell}}$  measured by the potentiostat and photocurrent  $I_{\text{PC}} = I_{\text{dark}} - I_{\text{light}}$  due to the illumination of the electrode. (c) Band diagram of the electrode and surface states in equilibrium with water, and definition of the electron affinity  $EA = E_{\text{vac}} - E_{\text{CBM}}$ , ionization energy  $E_i = E_{\text{vac}} - E_{\text{VBM}}$ , and band bending  $BB(\eta) = E_F(\text{FBP}) - E_F(\eta)$  for a given flat band potential (FBP) and applied potential  $\eta$ . The positions of the surface states are deduced from X-ray absorption spectroscopy as detailed in Fig. S1 in Supplemental Material [36].

properties similar to those of polycrystalline BDD, while exhibiting increased charge transfer reactions at the interface due to nanostructuring [19,43–45].

The BDD electrodes are studied as the working electrode (WE) in the three-electrode PEC cell presented in Fig. 1(a). The measurements are done in 3M KCl electrolyte, ensuring good ionic conductivity and limiting the influence of the diffusion processes in the Helmholtz layer. CV characterization of the electrodes can be found in the Supplemental Material [46]. While the potential and current are controlled by a potentiostat, the modulated illumination (1.8 Hz) of the WE at a chosen energy is set by a monochromator. The photocurrent is extracted either directly from the cell current recorded by the potentiostat, as presented in Fig. 1(b), or by the use of lock-in detection, enabling great sensitivity to small photocurrents down to picoamperes. The photocurrent is not capacitive, and no spikes are observed. In contrast to the cell current, the photocurrent is considered positive when it flows from the counter electrode (CE) to the WE, accounting for the solvated electron current as positive. Since the photocurrent is much smaller than the overall cell current, the effect of light excitation on the band bending and polarization of the electrode is considered negligible in the following discussion.

The band alignment at the diamond/water interface is presented in Fig. 1(c). At the surface, the energy difference between the conduction band minimum (CBM) and the local vacuum level  $E_{\text{vac}}$  is defined as the surface electron

affinity (EA) and strongly depends on the surface termination, which results in a surface dipole that shifts the local vacuum level [25,47,48]. The position of the valence band maximum (VBM) at the surface is 5.47 eV below the bulk CBM, corresponding to the band gap of diamond. In the bulk, the Fermi level  $E_F$  at equilibrium is pinned to the level of the doping states, in our case about 0.39 eV above the VBM [49]. The equilibrium of this Fermi level with the chemical potential of the electrolyte (dashed green line) leads to a surface charge transfer, the formation of a space-charge region at the surface of the diamond, and an associated surface band bending (solid green lines) [50]. This charge transfer is responsible for the surface conductivity of hydrogenated diamonds in water as the VBM is above the Fermi level at the surface [52–55].

When a potential  $E_{\text{WE}}$  is applied, the Fermi level shifts accordingly in the bulk BDD electrode by a value  $\eta$  (dashed red line) and thus modifies the surface band bending (solid red lines).  $\eta$  cannot be directly measured as  $E_{\text{WE}}$  because of Ohmic drops and contact potentials in the real PEC cell. However, only a negligible fraction of any applied potential appears across the Helmholtz layer [56], and the remaining difference can be measured as explained in Refs. [50,57].

The EA of the surface can be determined by measurement of the ionization energy  $E_i$  by photoelectron yield spectroscopy (PYS) [58]; see Fig. S6 and Table S1 in Supplemental Material [59]. In contrast to UV photoelectron spectroscopy and X-ray emission spectroscopy,

which are performed under vacuum, PYS is conducted at atmospheric pressure with adsorbed water molecules. The contact with these adsorbed molecules is sufficient to induce charge transfers similar to those observed between the electrode and the redox couples (involving oxygen and water) in the electrolyte [52]. The ionization energy and EA measured in this manner are assumed to remain valid in the electrolyte and are discussed further later. In contrast to most semiconductors, diamond electrodes have molecular surface states due to their termination. These states can exist within the band gap, where electrons can be excited upon light excitation, and, similarly to surface defects, they can lead to charge trapping [25,62,63].

The position of these surface states can be determined by X-ray absorption spectroscopy (XAS), as presented in Fig. 2(a) and summarized in Fig. 1(c). The large absorption above 289.5 eV is due to the excitation of core C 1s electrons to the diamond's conduction band (CB) [37]. The sharp peak at 289.3 eV is related to the excitation of the core exciton, which is a bound state between the electron excited to the CB and the associated core hole. Below, the different features correspond to the transitions of C 1s electrons to  $\pi_{\text{C}=\text{O}}^*$ ,  $\sigma_{\text{C}-\text{H}}^*$ , and  $\sigma_{\text{C}-\text{OH}}^*$  surface groups, at energies of 286.5 eV [39], 287.8 eV [40], and 288.7 eV [41], respectively. H-BDD exhibits a distinct absorption peak corresponding to the C—H termination. However, exposure to air before measurement has already led to some oxidation of the surface, as evidenced by signals at 286.5 eV and possibly at 288.7 eV. This spontaneous oxidation of the surface is explained in Sec. II C. In comparison, O-BDD absorbs less at 287.8 eV and more at 286.5 eV, signifying a greater degree of surface oxidation. The pre-edge X-ray absorption of F-BDD also shows the signature of oxygenated surface groups, but the overall absorption in this region is significantly reduced because C—F surface groups are located above the band gap [37,38] (see Supplemental Materials for details [36]).

The associated charge transfers due to direct photoexcitation or charge trapping have been identified in air by surface photovoltage measurements [25], but their role in the photoelectrochemical properties of diamond electrodes has not yet been precisely identified. In the following, we use the lower number of surface states within the band gap of F-BDD compared with the other samples to identify the photocurrent due to surface states by comparing these three surface terminations.

The incident-photon-to-current efficiency (IPCE) measured on the BDD with H, O, and F terminations as a function of the applied potential and excitation photon energy is shown in Figs. 2(b)–2(d). While the H termination was achieved by a plasma, O and F were obtained wet-chemically. For all surface chemistries, stronger photocurrent is observed above the band gap (5.47 eV) due to direct band-to-band excitation. However, a significant photocurrent is also observed below the band gap for O-BDD and

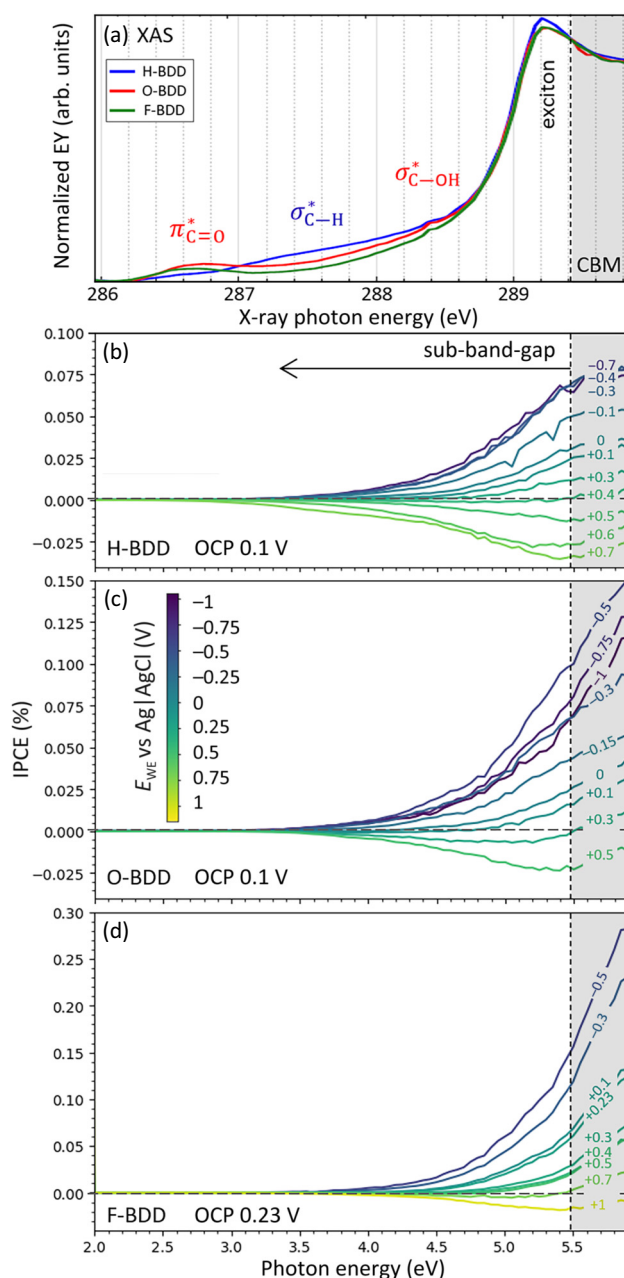


FIG. 2. Effect of diamond surface termination on photocurrent. (a) XAS spectra at the C *K*-edge for H-BDD (blue), O-BDD (red), and F-BDD (green). IPCE recorded on H-BDD (b), O-BDD (c), and F-BDD (d) in 3M KCl electrolyte for different applied potentials vs the Ag|AgCl reference electrode. The color scale is the same in (b)–(d) for easier comparison, but the potential ranges applied to the different samples have been adjusted to account for their different band bending and OCP characteristics, which depend on surface chemistry. The vertical dashed lines correspond to the band gap energy. EY, electron yield.

H-BDD, starting from about 3.5 eV, as previously observed [25]. In contrast, F-BDD shows a much-reduced sub-band-gap photocurrent, regardless of the applied potential. Sub-band-gap photocurrent is indeed strongly related to the

presence of hydroxylated and hydrogenated surface states within the diamond band gap, as illustrated in Fig. 1(c). The photoexcitation of  $sp^2$  surface states has often been considered as a possible origin of photocurrent [32,64]. However, F-BDD shows more  $sp^2$  surface states than O-BDD and H-BDD (see Fig. S1 in Supplemental Material [36]), challenging this hypothesis. Furthermore,  $sp^2$  surface states are excited at 0.7 eV and at around 1.5 eV [25], while no photocurrent is measured below 3.5 eV. Similarly, the excitation of  $\pi_{C=O}^*$  surface states, between 2.25 and 3.3 eV [25], can be ruled out.

For applied potentials between  $-0.3$  and  $+0.5$  V vs Ag|AgCl, the photocurrent observed on H-BDD and O-BDD is nearly identical, despite the measurements starting at the open circuit potential (OCP) to limit electrochemical modification of the surface. This suggests the spontaneous oxidation of the H-BDD surface upon contact with water, as previously identified by near ambient pressure X-ray photoelectron spectroscopy [19]. The reason for this spontaneous oxidation is discussed later.

### B. Photoredox reactions and emission of solvated electrons

To determine the origin of the photocurrent, we quantified the amount of solvated electrons emitted by O-BDD over 1 h of constant light exposure as a function of applied potentials by fluorimetry [65] (see Fig. S7 in Supplemental Material for details [66]). Briefly, a small amount of  $\text{NO}_3^-$  is added to the electrolyte, which plays the role of electron scavenger to form  $\text{NO}_2^-$ . After the experiment, the electrolyte is recovered and reacted with 2,3-diaminonaphthalene (2,3-DAN), which in the presence of  $\text{NO}_2^-$  undergoes a diazotation reaction to form the very sensitive fluorescent probe 1*H*-naphthotriazole. The  $\text{NO}_2^-$  concentration allows the quantification of the solvated electron concentration, as shown in Fig. 3(b). A control experiment is performed in the dark at  $-0.5$  V (left dashed bar) to demonstrate that no  $\text{NO}_2^-$  is generated electrochemically as the amount detected by fluorescence corresponds to the detection limit (see Fig. S7 in Supplemental Material [66]). At 0.1 V, for excitation at 4.5 eV, below the band gap (central dashed bar), no solvated electrons were detected, as there is no detectable difference compared with the control experiment. Hence, the photocurrent measured below the band gap is only due to the excitation and redox reaction of the surface groups. For excitation above the band gap, the amount of solvated electrons increases for more negative potentials and depends strongly on the surface band bending.

The surface band bending can be estimated as the difference between the applied potential and the flat band potential (FBP). A usual way to determine the FBP of classical semiconductor electrodes, known as Gärtner-Butler analysis, is to plot the photocurrent intensity generated by

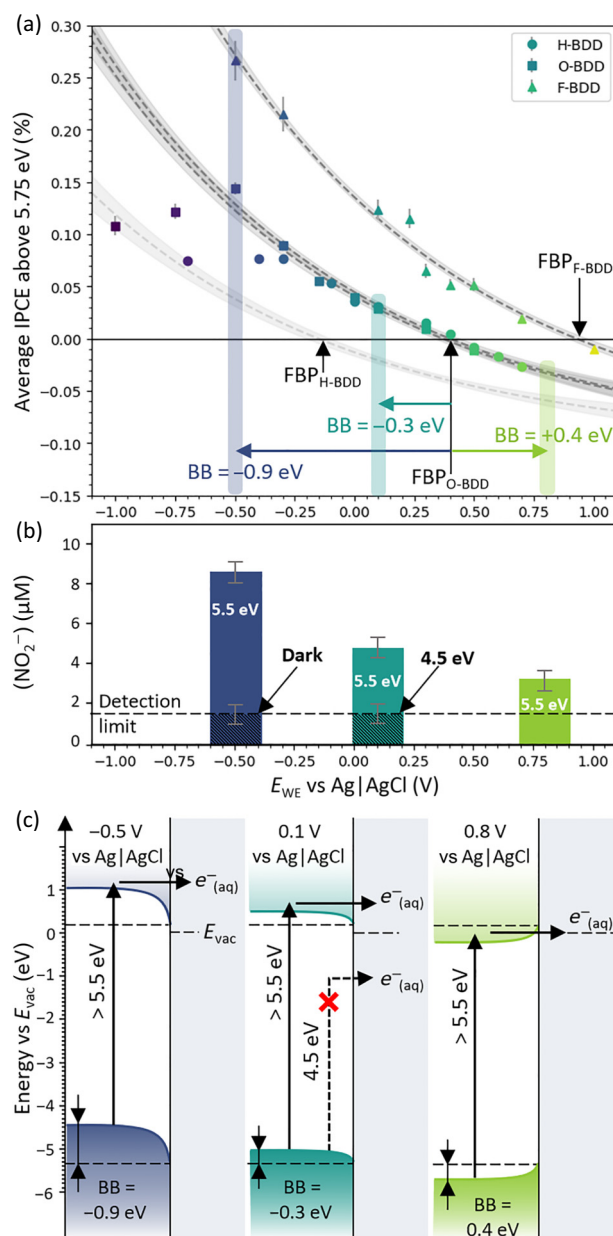


FIG. 3. Photoexcitation of diamond electrodes above the band gap. (a) Average IPCE for excitation above 5.75 eV at different potentials for H-BDD (circles), O-BDD (squares), and F-BDD (triangles). The dashed lines correspond to fits considering Schottky barrier models for different FBPs (black arrows). Colored arrows show the band bending observed under the conditions used for dosing the solvated electrons. (b)  $\text{NO}_2^-$  concentration measured by fluorimetry, which relates to the amount of emitted solvated electrons. (c) Schemes for the origin of the solvated electrons depending on the band bending and the excitation energy. The EA (determined by PYS measurement as in Fig. S6 in Supplemental Material [59]) and the FBP correspond to the O-BDD sample.

excitation above the band gap with respect to the applied potential, as represented in Fig. 3(a) [67]. The dashed dark gray lines correspond to a Schottky barrier model fitted to

the data. A Schottky behavior is expected when the current is limited not by chemical processes or by ion diffusion in solution, but only by the rate at which the excited carriers approach the surface [2,56]. These assumptions are valid here because the emission of solvated electrons from the diamond surface is not mediated by any chemical reaction and the ion concentration in solution is large. The photocurrent is thus determined as [56]

$$I_{\text{PC}} = I_{\text{PC}}^0 [\exp(-\eta q/nkT) - 1], \quad (1)$$

with  $I_{\text{PC}}^0$  the saturation current,  $\eta \simeq E_{\text{WE}} - \text{FBP}$  the applied potential expressed with respect to the FBP,  $q$  the elementary charge,  $k$  the Boltzmann constant,  $T$  the temperature, and  $n$  the ideality factor, which accounts for the recombination of charge carriers. Simply, at the FBP, the photocurrent is close to zero because there is no driving force to separate the photogenerated charge carriers. When a negative potential is applied, the electric field in the space-charge region increases, increasing the separation of electron-hole pairs and driving the electrons in the conduction band toward the surface of the diamond.

The Schottky barrier model is fitted to the O-BDD, H-BDD, and F-BDD data, changing only the FBP, which is dependent on the surface states. The IPCE corresponding to the saturation current is  $(0.10 \pm 0.02)\%$ . The ideality factor,  $n = 43 \pm 5$ , is very large, showing a significant recombination of charge carriers, strongly reducing the emission yield. The defects in the electrode leading to the observed charge recombination are particularly important on polycrystalline nanostructured BDD because of the grain boundaries and local defects due to etching of the surface and doping. The FBPs of H-BDD and O-BDD are  $0.37 \pm 0.03$  V and  $0.40 \pm 0.04$  V, respectively. It is again evident that both surfaces are very similar due to the spontaneous surface oxidation of H-BDD in water. The FBP of F-BDD is much larger,  $0.93 \pm 0.04$  V, because the EA of the fluorinated surface is larger, as measured by PYS; see Fig. S6 in Supplemental Material [59]. For potentials below  $-0.3$  V vs Ag|AgCl, one can observe that the measurements diverge from the theoretical curves [dashed lines in Fig. 3(a)] in the case of O-BDD and H-BDD. At these negative potentials, the surface undergoes electrochemical reduction, as discussed in more detail later, and these points were not considered for the fit. As a consequence, the EA and FBP are reduced, leading to a shift in the theoretical curve to the left until it reaches that of a fully hydrogenated surface [dashed light gray curve in Fig. 3(a)] with an FBP of about  $-0.15$  V.

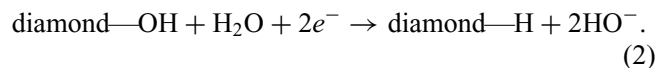
The three colored arrows correspond to the band bending at the potentials applied on O-BDD for which the solvated electrons were quantified. As illustrated in Fig. 3(c), downward band bending of  $-0.9$  and  $-0.3$  eV is observed at  $-0.5$  and  $+0.1$  V (OCP) vs Ag|AgCl, respectively,

favoring the emission of solvated electrons. Solvated electrons are also measured at  $0.8$  V vs Ag|AgCl, although this corresponds to an upward band bending of  $+0.4$  eV.

Upward surface band bending could also be induced by nitrogen doping. The higher doping state level raises the Fermi level in the bulk electrode. Electrons from the doping states, about  $1.7$  eV below the CBM, can be excited by visible light from about  $730$  nm. The nitrogen atoms naturally contained in detonation nanodiamonds may then explain their ability to emit solvated electrons in water under visible light illumination [17,21]. Similarly, it was shown recently that shallow nitrogen-vacancy centers can also be excited to produce a photocurrent response for wavelengths up to  $594$  nm [68]. Finally, nitrogen-doped ultrananocrystalline diamond has a near-infrared response, which is particularly useful for neuronal interfacing, and is also influenced by the surface termination [31,69,70].

The effect of surface termination on the sub-band-gap photoredox reaction was then investigated. Fluorination is an efficient technique to passivate the diamond surface and suppress most of the intraband surface states [37]. Hence, F-BDD was used as a reference to isolate the sub-band-gap contribution to the photocurrent on H-BDD and O-BDD. Difference photocurrent spectra, subtracted for a similar band bending, are shown in Fig. 4(a). These spectra were fitted by four Gaussian functions as shown in Figs. 4(b) and 4(c) at energies of  $4.19 \pm 0.1$  eV (blue),  $4.83 \pm 0.1$  eV (green),  $4.8 \pm 0.2$  eV (yellow), and  $5.38 \pm 0.1$  eV (red), attributed to single-photon photoexcitation [71]. More details about this procedure can be found in Fig. S5 in Supplemental Material [72].

For downward band bending, the photocurrent is positive, corresponding to photoreduction reactions of the oxidized surface states, forming C—H terminations:



The fit of the photocurrent shows two photoexcitation processes, at around  $4.2$  and  $4.8$  eV [blue and green in Fig. 4(b)], labeled “C—OH (1)” and “C—OH (2)” in Fig. 4(d). These energies correspond to the excitation of valence band (VB) electrons to the C—OH unoccupied surface states measured by XAS [see Fig. 2(a) and Fig. S1 in Supplemental Material [36]] as well as the transitions  $E_1$  and  $E_2$  at  $4.2$  and  $4.9$  eV previously reported in air [25]. The difference in energy observed between these two states could be due to the (de)protonation of the hydroxyl group in water or to a different oxygen bonding configuration, such as ether or carboxyl groups, especially on acid-treated surfaces [73].

For upward band bending, the photocurrent is negative, corresponding to photooxidation of the surface according to the opposite reaction. The fit of the photocurrent shows a single photoexcitation at around  $4.8$  eV [yellow

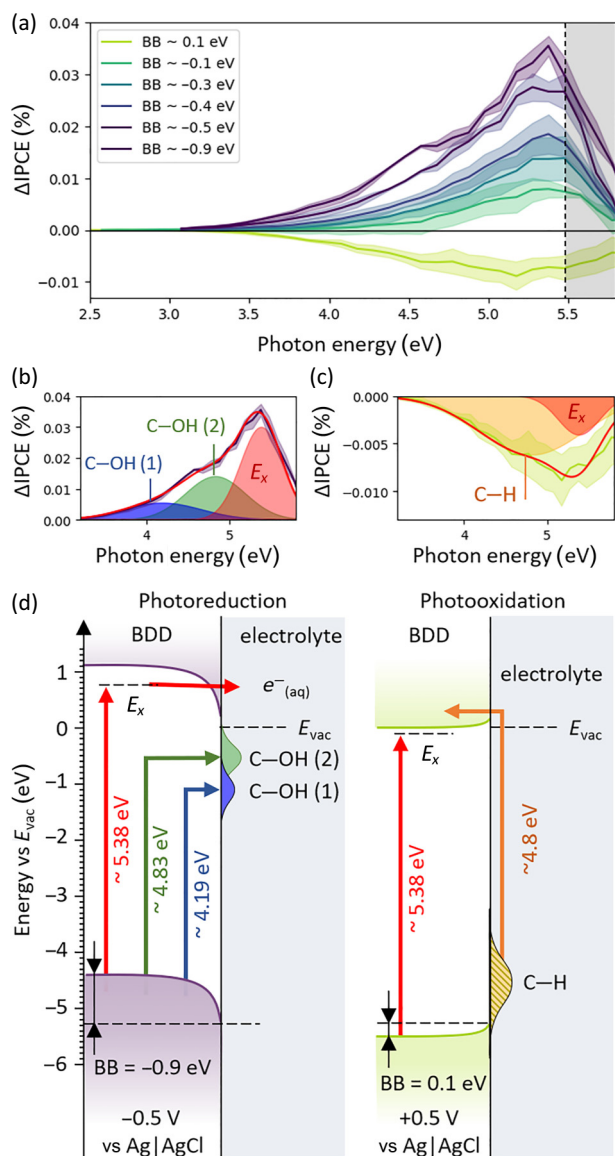


FIG. 4. Photoexcitation of diamond electrodes below the band gap. (a) Difference ( $\Delta$ IPCE) between the photocurrent measured on O-BDD/H-BDD and the photocurrent measured on F-BDD for a similar band bending. Fit of  $\Delta$ IPCE corresponding to band bendings of (b)  $-0.9$  eV and (c)  $0.1$  eV according to the four identified resonant photoexcitations represented in (d) involving C—OH surface states and excitonic states ( $E_x$ ).

in Fig. 4(c)], corresponding to the excitation of electrons from the C—H occupied surface states to the CB as represented in Fig. 4(d). In air, this transition was also detected between  $4.6$  and  $4.8$  eV [25].

The amplitudes of these components strongly depend on the band bending (see Fig. S5 in Supplemental Material [72]). A downward band bending favors the photoreduction reactions by pulling the holes away from the surface, thereby limiting charge recombination, while an upward band bending favors the photooxidation reactions by pulling electrons away from the surface.

The fourth process occurring at around  $5.4$  eV (red) corresponds to the excitation of electrons from the VB to an excitonic state of the CB. More precisely, its energy appears close to  $E_g - E_x - h\nu_{TA} = 5.32$  eV, where  $E_g$ ,  $E_x$ , and  $h\nu_{TA}$  are the energies of the band gap ( $5.47$  eV), of the indirect exciton ( $0.07$  eV), and of the transverse acoustic phonon ( $0.083$  eV) [25,74–76]. This process is stronger on O-BDD than on F-BDD, possibly because the exciton formation and/or dissociation depends on the surface termination, as observed in air [25]. When the exciton dissociates, charge separation is induced by the surface band bending, leading to a positive photocurrent for downward band bending and a negative photocurrent for upward band bending (see Fig. S5 in Supplemental Material [72]).

### C. Redox surface reactions probed by photocurrent measurements

When diamond surfaces are used for electrochemistry, possible reduction or oxidation of the surface must be considered depending on the electrochemical conditions. The oxidation and reduction significantly impact the interface properties by altering the EA, the band bending, and the double layer. While it is particularly difficult to characterize the interface of an electrode *operando* [77], we propose to determine the FBP from PC-CV measurements, and to use this physical quantity to monitor the level of oxidation of the surface depending on the applied potential.

PC-CV experiments were performed under constant illumination with an excitation energy of  $3.2$  eV, with the use of a tunable light-emitting diode (LED) source in  $0.5M$  KCl. Figure 5(a) presents the first three cycles of the CV measured on O-BDD, showing the surface capacitive behavior typical of the BDD electrode [19]. The cycles are largely repeatable, indicating good surface stability. Except for limited water reduction happening below approximately  $-0.4$  V vs Ag|AgCl, no clear redox peaks are observed because no redox couple was introduced into the electrolyte, and the decrease in cell current after the first cycle at negative potentials is likely due to the initial reduction of oxygen present in the solution. A small photocurrent (less than  $20$  nA) due to the modulated illumination is also observed [inset in Fig. 5(a)] but does not alter the electrochemical behavior of the electrode. The sub-band-gap excitation suggests that the photocurrent originates from the excitation of the surface states. As just demonstrated, the amplitude and sign of this photocurrent are directly correlated with the surface band bending.

Figure 5(b) shows the photocurrent along the cyclic voltammogram extracted from the third cycle. Details about the reconstruction of the PC cyclic voltammograms are given in Supplemental Material [78]. The more positive (negative) the applied potential, the more negative (positive) the photocurrent, as the upward (downward) band

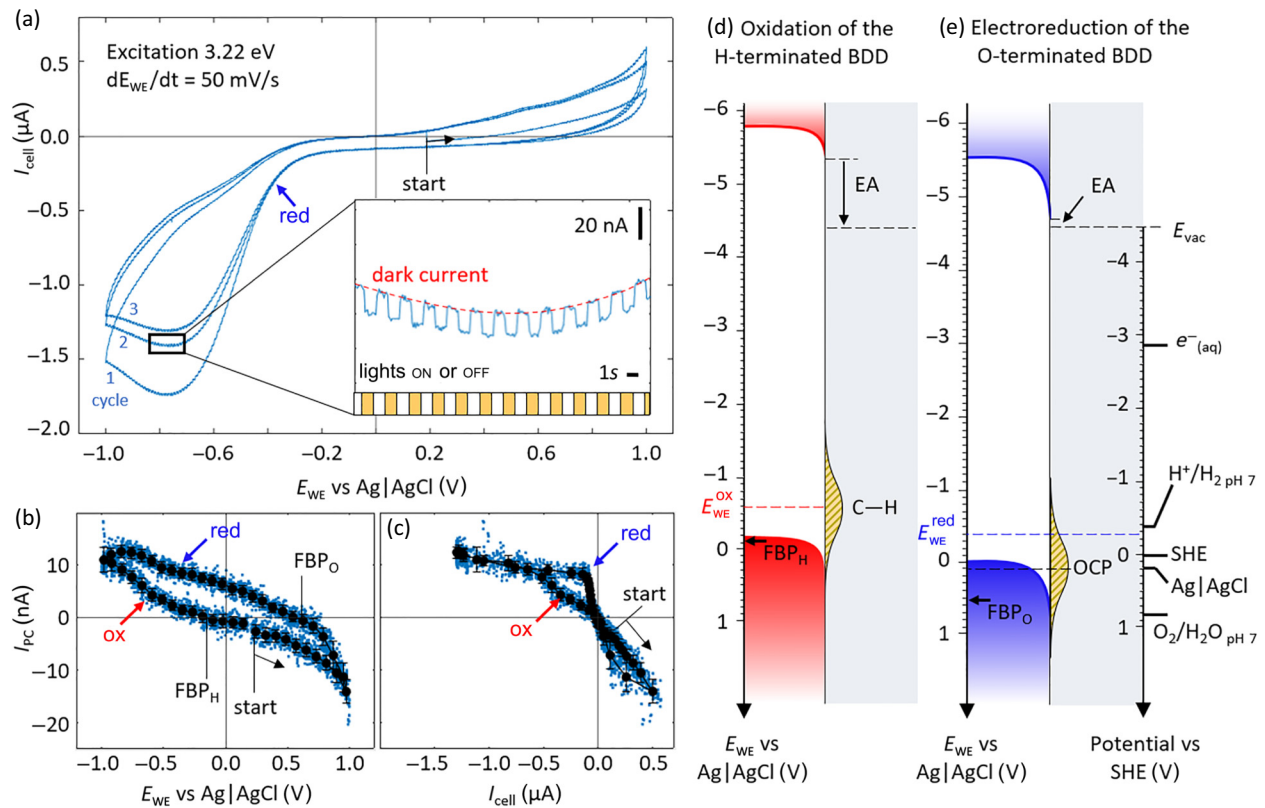


FIG. 5. Probing surface redox reactions on diamond with photocurrent. (a) CV of O-BDD between  $-1$  and  $1$  V vs Ag|AgCl (starting positively from the OCP measured in the dark) at a scan rate of  $50$  mV/s. Numbers indicate the first, second, and third cycles. The inset shows an enlargement of the photocurrent modulation ( $I_{\text{PC}} = I_{\text{dark}} - I_{\text{light}}$ ). PC-CV showing (b) the extracted photocurrent along the third CV cycle and (c) corresponding photocurrent-current plot. Black dots represent the local average values. The arrows labeled “red” and “ox” indicate the starting points of the electrochemical reduction and spontaneous oxidation of the surface. Potential diagrams at the diamond/water interface in the case of (d) an electrochemically reduced surface and (e) an oxidized surface at the applied potentials of “ox” and “red,” respectively. The EA of the surface is deduced from the measured ionization energy  $E_i$ . The  $E_{\text{WE}}$  scale is aligned with the potential vs the SHE in the electrolyte with use of the correction of the potential drop calculated in Supplemental Material Ref. [57].

bending is increased. The FBP can be measured when the photocurrent is zero. The hysteresis observed is a direct indication of the change in the surface oxidation level, modifying the EA and the FBP.

When the measurement starts, the electrode surface is already partially oxidized, and oxidizes further as the potential is increased. After the reverse potential is reached, the potential is decreased again until the photocurrent cancels. This corresponds to the FBP of the oxidized surface:  $\text{FBP}_{\text{O}} = +0.52 \pm 0.05$  V. This value is slightly more positive than the value determined by the Schottky barrier model in Fig. 3(a), as the electrochemical oxidation is more pronounced compared with the wet chemical oxidation in an acidic medium. Upon further decrease of the potential, below approximately  $-0.4$  V vs Ag|AgCl, the surface is hydrogenated again as seen in the previous section. Hence, the FBP measured in this second half of the cycle is the one of the hydrogenated surface:  $\text{FBP}_{\text{H}} = -0.11 \pm 0.01$  V. While this observation of the

FBP hysteresis demonstrates the oxidation and reduction of the surface of the diamond, further understanding of the processes involved would help to determine the stability of the surface termination depending on the conditions.

Figure 5(e) shows the potential diagram at the oxidized diamond/water interfaces under the condition when the reduction happens (approximately  $-0.4$  V vs Ag|AgCl). The EA of the surface of  $-0.15$  eV is deduced from the measured ionization energy  $E_i$  presented in Table S1 in Supplemental Material [59]. The position of the Fermi level in the bulk of the electrode is set by the doping level about  $0.39$  eV above the VBM. In contrast to usual band energy diagrams, the left scale corresponds to the applied potential ( $E_{\text{WE}}$ ) and is aligned with the right scale, corresponding to the absolute potential in the electrolyte, by correction of the potential drops as detailed in Supplemental Material Ref. [57]. It therefore translates into a potential diagram. In this way, it appears clear that the oxidized surface starts to reduce when  $E_{\text{WE}}^{\text{red}} = -0.4$  V vs Ag|AgCl

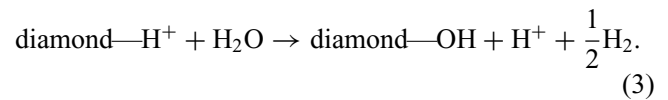
(dashed blue line) because the Fermi level reached the redox potential of  $\text{H}^+/\text{H}_2$  at  $\text{pH} \sim 7$  [ $-0.414$  V vs the standard hydrogen electrode (SHE) according to the Nernst equation] and that reduction of water occurs. This reduction is also observed directly in the cyclic voltammogram and indicated by a blue arrow. Water reduction usually proceeds via the formation of hydrogen radicals, which might attack the O surface terminations, ultimately leading to a H-terminated surface. The binding energy of hydrogen atoms on diamond is quite large (up to 3 eV [79], compared with approximately 0 eV for Pt [80]), meaning that their recombination to form molecular hydrogen is very unfavorable. This might explain why diamond materials are poor hydrogen evolution catalysts.

The oxidation of the surface is particularly hard to observe on the cyclic voltammogram. No clear feature is observed in the anodic range. In contrast to the previous case, no major redox couple of the electrolyte is involved as the applied potentials are not sufficiently high to drive water oxidation.

It is possible to increase the sensitivity of the PC-CV to redox reactions by plotting the photocurrent vs  $I_{\text{cell}}$  [Fig. 5(c)]. In conventional CV, the increase in current due to redox reactions happens simultaneously with other processes, such as the variation of the band bending and charge diffusion in the electrolyte, leading to broad peaks. Plotting the photocurrent vs  $I_{\text{cell}}$  enables the isolation of the purely redox reactions as they impact only  $I_{\text{cell}}$  but not the photocurrent, everything else being constant. For instance, the very broad current increase due to water reduction labeled “red” in the cyclic voltammogram appears extremely sharp in this plot (blue arrow), helping to determine the reaction onset. In contrast, no evolution of the photocurrent is observed in Fig. 5(b) at that potential, confirming that the electrochemical nature of the reduction reaction does not impact the photocurrent.

In the other half of the cycle, a smaller transition labeled “ox” can be observed at  $-0.6$  V vs Ag|AgCl, which we attribute to the onset of oxidation of the surface. Detection of the start of the surface oxidation at such a low potential may appear surprising at first as the applied potential is more negative than the onset potential of water reduction. Nevertheless, this again confirms that this process is not related to the oxidation of water. To better visualize the oxidation process of the surface, Fig. 5(d) shows the band alignment at  $-0.6$  V vs Ag|AgCl. The EA of the hydrogenated surface of  $-0.86$  eV is deduced from the measured ionization energy  $E_i$  presented in Table S1 in Supplemental Material [59]. As previously reported, the position of the Fermi level in the bulk of the electrode is set by the doping level about 0.39 eV above the VB, and the left scale is the applied potential ( $E_{\text{WE}}$ ) corrected for the potential drop in the cell. The reduced surface starts to oxidize at  $E_{\text{WE}}^{\text{ox}} = -0.6$  V vs Ag|AgCl (dashed red line), when the Fermi level drops below the level of the occupied

C—H surface states, leading to charge transfer and favoring the oxidation of the surface, according to the following proposed equation:



For potentials between  $-0.6$  and  $-0.4$  V, both phenomena happen simultaneously: electroreduction of water tends to reduce the surface, while charge transfer from the C—H surface states tends to oxidize the surface. Partial oxidation of the surface also diminishes the negative EA of the surface and lower the energy position of the C—H states until an equilibrium is reached. The more the surface oxidizes, the lower is the energy of the C—H surface states, and the stabler they become.

These results also demonstrate why the diamond surfaces spontaneously oxidize in contact with water and why fully hydrogenated BDD surfaces can exist only at potentials below  $-0.6$  V vs Ag|AgCl. Without any applied potential, the Fermi level of the diamond surface is in equilibrium with the water and corresponds to the OCP usually measured at around  $+0.1$  V vs Ag|AgCl (see Sec. II A). Because the Fermi level is well below the C—H surface states, charge transfer occurs and the surface groups spontaneously oxidize until a new equilibrium is reached. The same happens in air by equilibrium with adsorbed molecules. While oxidization is occurring, the EA of the surface increases, shifting the position of the remaining occupied C—H states until they match with the Fermi level. The oxidation of the surface is hence self-limited. In particular, the remaining C—H groups of O-BDD are stable because the EA of this surface is about 0.7 eV lower than that of the hydrogenated surface, matching the OCP [Fig. 5(e)].

This equilibrium also depends on the chemical potential in the electrolyte and thus on the pH. Lowering the pH shifts the equilibrium potential according to the Nernst equation ( $-59.2$  mV/pH) and further stabilizes the hydrogenated surface [14]. Consequently, electrochemical oxidation appears more efficient than acidic treatment in removing diamond hydrogen termination in aqueous media. However, to obtain a fully hydrogenated surface under our conditions without an applied potential, the pH would need to be far below 0, making these considerations and the Nernst equation irrelevant. Conversely, when a hydrogenated diamond surface is put in water, its oxidation leads to a decrease of the pH of the electrolyte [8,52].

### III. CONCLUSION

In this study, we have demonstrated that charge transfer reactions at the diamond/water interface can be precisely modulated by applying an external potential and photoexcitation.

A PC-CV technique enabled us to probe fundamental properties of the diamond surface termination directly in liquid and under a potential. This technique could be applied to probe functionalized diamond and other semiconductor electrodes in the future. Electrochemically induced surface redox reactions, which lead to the formation of hydroxylated or hydrogenated surfaces, can be used to control the electron affinity and adjust the band bending at the diamond/electrolyte interface. However, the hydrogenated surface of BDD is unstable in water and spontaneously oxidizes until a new equilibrium is reached, depending on the electron affinity and the pH of the solution.

The electrochemical tuning of band bending and surface chemistry allows fine control of the photoexcitation of the electrode. Resonant photoexcitation of electronic transitions in the UV-visible range enables controlled photochemical reactions at the diamond/water interface. The emission of solvated electrons has been evidenced for excitation above the band gap and can be modulated by tuning of the surface band bending. We have shown that BDD electrodes behave like Schottky barriers, with the potential barrier being tunable by the surface states. The observed large amount of charge recombination provides room for increasing the incident-photon-to-current efficiency. The steady progress in the synthesis of defect-free single-crystal diamonds could help mitigate the effect of the large amount of charge recombination. Other strategies, such as surface passivation and interface engineering, could also help suppress this recombination and increase efficiency.

A comprehensive understanding of the interfacial photochemical and electrochemical processes on BDD electrodes in equilibrium with the electrolyte paves the way for new engineered solutions. Rational design of novel diamond-based electrodes may open new avenues for photoelectrochemical generation of solar fuels, water remediation, plastic reforming reactions, or even photorechargeable energy storage devices. For instance, functionalizing the diamond surface with appropriate molecules, altering the aqueous microenvironment (pH, redox couples, etc.), or doping the diamond with heteroatoms other than boron may enable photoreactions in the visible range without the necessity of applying any external potential.

## IV. METHODS AND MATERIALS

### A. Nanostructured boron-doped diamond

The electrodes are made from a polycrystalline boron-doped diamond wafer nanostructured by reactive ion etching after dewetting of a metal mask. The average doping is 5700 ppm ( $10^{21} \text{ cm}^{-3}$ ) [18]. The hydrogen termination (referred to as “H-BDD”) is initially obtained by exposure of the sample to hydrogen plasma treatment at a temperature of 700 °C. The oxidized termination (referred to as

“O-BDD”) is obtained by wet chemical treatment in a mixture of concentrated sulfuric acid and nitric acid (ratio 3:1) for 1.5 h at elevated temperatures, about 250 °C.

### B. Fluorination procedure

**CAUTION:** Elemental fluorine and anhydrous hydrogen fluoride (aHF) are highly toxic and can cause severe injuries by skin and eye contact or inhalation. Therefore, all manipulations of these chemicals have to be performed under a well-ventilated fume hood. The wearing of protective gloves, an apron, and a head screen is strongly recommended. All apparatus must be checked carefully for any leaks before any reactions are started.

Fluorinated termination (referred to as “F-BDD”), is obtained by fluorination in liquid HF containing 30% elemental fluorine and subsequent removal of volatile perfluorinated hydrocarbons by evaporation under a vacuum. Elemental fluorine and anhydrous HF were obtained from Solvay Fluor GmbH and used as received.

Fluorine and anhydrous HF were kept in stainless-steel lines of known volume equipped with capacitance pressure gauges (type 280E, Setra Instruments, Acton, Massachusetts, USA) and with bellow valves (Balzers BPV25004 and Nupro Swagelok SS4BG), as well as with Gyrolok and Cajon fittings. Fluorination reactions in anhydrous HF were performed in 100 mL reactors consisting of a perfluoroalkoxy alkane (PFA) bulb with an NS29 socket standard taper (Bohlander, Lauda, Germany) connected to a PFA NS29 cone standard taper and a PFA needle valve (Galtek 204-30, Fluoroware, Chaska, Minnesota, USA). The parts were held together with a metal compression flange.

A 100 mL PFA round-bottom flask reactor equipped with a magnetic stirring bar was charged with the diamond sample and 10 ml of anhydrous HF. The suspension was stirred and cooled to  $-78 \text{ }^\circ\text{C}$ , and a vacuum was applied for 5 min. Elemental fluorine (3.3 mmol, 40 mol%) was added at  $-78 \text{ }^\circ\text{C}$ . The suspension was warmed to 50 °C and stirred for 5 days. After the removal of HF and all other volatiles under reduced pressure, the diamond was dried in a vacuum until all volatile fluorinated side products were removed.

### C. X-ray absorption spectroscopy

XAS was performed at the BESSY II synchrotron in Berlin on the U49/2-PGM1 undulator beamline with use of the ultrahigh vacuum LiXEdrom experimental station, described in detail elsewhere [76]. The measurements were conducted in the electron yield mode, where the incident photon energy was swept and the drain current, due to the emitted electrons from the sample, was simultaneously recorded by a Keithley 6514 ammeter. The spectra were normalized by the incident photon flux between 286 and 290.5 eV. The energy resolution of the monochromator

in the range of the C 1s (approximately 285 eV) X-ray absorption edges was approximately 75 meV.

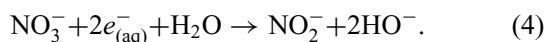
#### D. Photocurrent spectroscopy

The BDD electrodes were used as the WE in a spectroelectrochemical flow cell (SEC-3F, C3-Analysentechnik). The electrode area was 0.8 mm<sup>2</sup>. It was contacted by copper tape via the doped silicon substrate used for the deposition. The low resistivity of the substrate (0.01–0.02 Ω cm) ensures the Ohmic contact. The CE was a stainless-steel tube with a surface area of approximately 75 mm<sup>2</sup>. The potential on the WE was set relative to an Ag|AgCl reference electrode with the use of an SP-200 potentiostat (Biologic), with the current recorded. A positive current indicated the flow of negative charge from the WE to the CE. All photocurrent measurements were performed in an aqueous 3M KCl electrolyte, transparent up to photon energies of approximately 5.9 eV. Modulated illumination was provided by a laser-driven light source (EQ-99X-CAL-S, Hamamatsu) with a custom quartz prism monochromator (T. Dittrich and S. Fengler), covering photon energies between 0.45 and 6.2 eV at a modulation frequency of 1.8 Hz. The FWHM achieved by the monochromator under working conditions is about 0.05 eV. The modulated photocurrent was measured with the use of a lock-in amplifier (EG&G 5210). The photocurrent spectra were normalized to light intensity measured in the same conditions with a S130VC photodiode power sensor from Thorlabs corrected from its responsivity. Because each spectrum acquisition takes about 1 h, partial oxidation of the hydrogenated surface is observed. To limit electrochemical modification of the surface upon measurement of the photocurrent spectra, each spectrum is recorded from the OCP toward the largest polarization where electrochemistry happens, as discussed in Sec. II.

For the dynamic measurement of the photocurrent on the cyclic voltammogram, a high-intensity LED at 3.22 eV (pE-4000, CoolLED) was used.

#### E. Fluorimetric titration of solvated electrons

The titration of solvated electrons was achieved by fluorimetry, with use of a protocol adapted from Ref. [64]. The setup was the same as for photocurrent spectroscopy, but instead of the use of a 3M KCl electrolyte, the KCl concentration was decreased to 0.1M to avoid interferences, and 2 mM KNO<sub>3</sub> (Sigma-Aldrich) was added. The NO<sub>3</sub><sup>-</sup> ions serve as scavengers for the solvated electrons to form NO<sub>2</sub><sup>-</sup> ions:



After 1 h of continuous illumination at a given applied potential and light energy, the electrolyte was recovered from the cell. From the approximately 100 μL contained in

the cell, 50 μL was taken and mixed with 25 μL of 0.48 mM 2,3-DAN (Sigma-Aldrich) solution (in 0.63 N HCl, Carl Roth). In this step, 2,3-DAN reacts with the NO<sub>2</sub><sup>-</sup> ion to form 1*H*-naphthotriazole.

After 10 min incubation in the dark and at room temperature, 25 μL of 1.32M NaOH solution was added to the mixture and the latter was further diluted with 1000 μL of 0.44M NaOH solution. Under these conditions, 1*H*-naphthotriazole exhibits a strong fluorescence signal at 405 nm when excited at 365 nm, as shown in Fig. S7(a) in Supplemental Material [66]. By comparing the fluorescence intensity measured at 405 nm with a calibration curve [Fig. S7(b) in Supplemental Material [66]] obtained with known amounts of NaNO<sub>2</sub> (in 0.1M KCl, Sigma-Aldrich), we could determine the NO<sub>2</sub><sup>-</sup> concentration in the cell with a precision of 0.1 μM.

The fluorimeter used in this study consisted of a UV-visible spectrometer (Ocean SR6, OceanOptics) coupled to a tunable LED light source (pE-4000, CoolLED) arranged in a 90° geometry. Since no filter was used to remove the elastically scattered light from the source, a strong peak can be observed at 365 nm in all fluorescence spectra, even in the absence of 2,3-DAN.

#### ACKNOWLEDGMENTS

This work was funded by a Freigeist Fellowship from the Volkswagen Foundation (No. 89592) and the Horizon 2020 project DIACAT (Contract No. 665085) of the European Commission. We thank Patricia Quellmalz, Dr Christian Giese, and Dr Johannes Ackermann for preparing the diamond surface electrodes. We are grateful to Dr Steffen Fengler and Dr Thomas Dittrich for their development of the photocurrent monochromator, and Dr Ronny Golnak for providing the UV-visible spectrometer used for fluorometry, which made this study possible. X-ray absorption spectroscopy was conducted at the BESSY II synchrotron on the LiXEdrom beamline with the assistance of Dr Ronny Golnak and Dr Jie Xiao. We also thank Dr Thomas Unold for providing access to the PYS measurement setup. The authors thank Solvay Fluor GmbH for generous donations of elemental fluorine and anhydrous HF.

A.C. was responsible for conceptualization, data curation (photocurrent spectroscopy and XAS), formal analysis, investigation, methodology, visualization, writing the original draft, and reviewing and editing the manuscript. L.G. contributed to data curation (solvated electron dosage), formal analysis, investigation, visualization, writing the original draft, and reviewing and editing the manuscript. M.R. handled data curation (photoelectron yield spectroscopy), formal analysis, and reviewing and editing the manuscript. M.D. provided resources for the fluorination of the BDD surface. M.F. contributed

resources for the fluorination of the BDD surface and participated in reviewing and editing the manuscript. P.K. was responsible for funding acquisition, resources for the production of nanostructured diamonds, and reviewing and editing the manuscript. A.K. contributed to funding acquisition, resources for the fluorination of the BDD surface, and reviewing and editing the manuscript. T.P. was responsible for conceptualization, funding acquisition, project administration, resources, writing the original draft, and reviewing and editing the manuscript.

The authors declare that they have no conflict of interest.

### DATA AVAILABILITY

The data that support the findings of this article are not publicly available upon publication because it is not technically feasible and/or the cost of preparing, depositing, and hosting the data would be prohibitive within the terms of this research project. The data are available from the authors upon reasonable request.

- [1] J. H. Montoya, L. C. Seitz, P. Chakthranont, A. Vojvodic, T. F. Jaramillo, and J. K. Nørskov, Materials for solar fuels and chemicals, *Nat. Mater.* **16**, 70 (2016).
- [2] Jenny Schneider, Detlef Bahnemann, Jinhua Ye, Gianluca Li Puma, Dionysios D Dionysiou, Jenny Schneider, Detlef Bahnemann, Jinhua Ye, Gianluca Li Puma, and Dionysios D Dionysiou, *Part 1 Fundamental Aspects of Photocatalysis* (The Royal Society of Chemistry, 2016).
- [3] Brian O'Regan and Michael Grätzel, A low-cost, high-efficiency solar cell based on dye-sensitized colloidal TiO<sub>2</sub> films, *Nature* **353**, 737 (1991).
- [4] Q. Guo, C. Zhou, Z. Ma, and X. Yang, Fundamentals of TiO<sub>2</sub> photocatalysis: concepts, mechanisms, and challenges, *Adv. Mater.* **31**, 50 (2019).
- [5] Guiji Liu, Fan Zheng, Junrui Li, Guosong Zeng, Yifan Ye, David M. Larson, Junko Yano, Ethan J. Crumlin, Joel W. Ager, Lin-wang Wang, and Francesca M. Toma, Investigation and mitigation of degradation mechanisms in Cu<sub>2</sub>O photoelectrodes for CO<sub>2</sub> reduction to ethylene, *Nat. Energy* **6**, 1124 (2021).
- [6] A. G. Tamirat, J. Rick, A. A. Dubale, W. N. Su, and B. J. Hwang, Using hematite for photoelectrochemical water splitting: a review of current progress and challenges, *Nanoscale Horiz.* **1**, 243 (2016).
- [7] Y. Piekner, D. S. Ellis, D. A. Grave, A. Tsyganok, and A. Rothschild, Wasted photons: photogeneration yield and charge carrier collection efficiency of hematite photoanodes for photoelectrochemical water splitting, *Energy Environ. Sci.* **14**, 4584 (2021).
- [8] W. A. Smith, I. D. Sharp, N. C. Strandwitz, and J. Bisquert, Interfacial band-edge energetics for solar fuels production, *Energy Environ. Sci.* **8**, 2851 (2015).
- [9] A. M. Ganose, D. O. Scanlon, A. Walsh, and R. L. Z. Hoye, The defect challenge of wide-bandgap semiconductors for photovoltaics and beyond, *Nature* **13**, 4715 (2022).
- [10] W. Jaegermann, B. Kaiser, J. Ziegler, and J. Klett, in *Photoelectrochemical Solar Fuel Production: From Basic Principles to Advanced Devices*, edited by S. Giménez and J. Bisquert (Springer International Publishing, Castello de la Plana, Spain, 2016), pp. 199–280.
- [11] J. H. T. Luong, K. B. Male, and J. D. Glennon, Boron-doped diamond electrode: synthesis, characterization, functionalization and analytical applications, *Analyst* **134**, 1965 (2009).
- [12] S. J. Cobb, Z. J. Ayres, and J. V. Macpherson, Boron doped diamond: a designer electrode material for the twenty-first century, *Annu. Rev. Anal. Chem.* **11**, 463 (2018).
- [13] M. Elisabeth and K. Anke, Surface control of nanodiamond: from homogeneous termination to complex functional architectures for biomedical applications, *Acc. Chem. Res.* **55**, 3594 (2022).
- [14] Yasuaki Einaga, Boron-doped diamond electrodes: fundamentals for electrochemical applications, *Acc. Chem. Res.* **55**, 3605 (2022).
- [15] B. F. Bachman, D. Zhu, J. Bandy, L. Zhang, and R. J. Hamers, Detection of aqueous solvated electrons produced by photoemission from solids using transient absorption measurements, *ACS Meas. Sci. Au* **2**, 46 (2022).
- [16] C. Saucedo, N. Rieders, and R. J. Hamers, Influence of hydrogen and oxygen surface termination on the mechanism of sub-bandgap photoelectron emission from diamond(111) into vacuum and into water, *Diamond Relat. Mater.* **153**, 112011 (2025).
- [17] F. Buchner, T. Kirschbaum, A. Venerosy, H. Girard, J.-C. Arnault, B. Kiendl, A. Krueger, K. Larsson, A. Bande, T. Petit, and C. Merschjann, Early dynamics of the emission of solvated electrons from nanodiamonds in water, *Nanoscale* **14**, 17188 (2022).
- [18] D. Zhu, L. Zhang, R. E. Ruther, and R. J. Hamers, Photoilluminated diamond as a solid-state source of solvated electrons in water for nitrogen reduction, *Nat. Mater.* **12**, 836 (2013).
- [19] P. Knittel, F. Buchner, E. Hadzifejzovic, C. Giese, P. Quellmalz, R. Seidel, T. Petit, B. Iliev, T. J. S. Schubert, C. E. Nebel, and J. S. Foord, Nanostructured boron doped diamond electrodes with increased reactivity for solar-driven CO<sub>2</sub> reduction in room temperature ionic liquids, *ChemCatChem* **12**, 5548 (2020).
- [20] L. Zhang, D. Zhu, G. M. Nathanson, and R. J. Hamers, Selective photoelectrochemical reduction of aqueous CO<sub>2</sub> to CO by solvated electrons, *Angew. Chem.* **126**, 9904 (2014).
- [21] T. Yoshikawa, H. Asakawa, T. Matsumoto, K. Ichikawa, A. Kaga, S. Yamamoto, R. Izumi, M. Ohno, T. Mahiko, M. Mutsuda, S. Yamasaki, and N. Tokuda, CO<sub>2</sub> reduction by visible-light-induced photoemission from heavily N-doped diamond nano-layer, *Carbon* **218**, 118689 (2024).
- [22] N. Roy, Y. Hirano, H. Kuriyama, P. Sudhagar, N. Suzuki, K. I. Katsumata, K. Nakata, T. Kondo, M. Yuasa, I. Serizawa, T. Takayama, A. Kudo, A. Fujishima, and C. Terashima, Boron-doped diamond semiconductor electrodes: Efficient photoelectrochemical CO<sub>2</sub> reduction through surface modification, *Sci. Rep.* **6**, 38010 (2016).
- [23] Z. Shpilman, I. Gouzman, T. K. Minton, L. Shen, A. Stacey, J. Orwa, S. Praver, B. C. C. Cowie, and A. Hoffman, A near

- edge X-ray absorption fine structure study of oxidized single crystal and polycrystalline diamond surfaces, *Diamond Relat. Mater.* **45**, 20 (2014).
- [24] M. Sobaszek, M. Brzhezinskaya, A. Olejnik, V. Mortet, M. Alam, M. Sawczak, M. Ficek, M. Gazda, Z. Weiss, and R. Bogdanowicz, Highly occupied surface states at deuterium-grown boron-doped diamond interfaces for efficient photoelectrochemistry, *Small* **19** (26), 2208265 (2023).
- [25] A. Chemin, I. Levine, M. Rusu, R. Vaujour, P. Knittel, P. Reinke, K. Hinrichs, T. Unold, T. Dittrich, and T. Petit, Surface-mediated charge transfer of photogenerated carriers in diamond, *Small Methods* **7** (11), 2300423 (2023).
- [26] K. Patel, K. Hashimoto, and A. Fujishima, Photoelectrochemical investigations on boron-doped chemically vapour-deposited diamond electrodes, *J. Photochem. Photobiol., A* **65**, 419 (1992).
- [27] A. Y. Sakharava, Y. V. Pleskav, F. Di Quarto, S. Piazza, C. Sunseri, I. G. Teremetskaya, and V. P. Varnin, Synthetic diamond electrodes: Photoelectrochemical investigation of undoped and boron-doped polycrystalline thin films, *J. Electrochem. Soc.* **142**, 2704 (1995).
- [28] L. Boonma, T. Yano, D. A. Tryk, K. Hashimoto, and A. Fujishima, Observation of photocurrent from band-to-band excitation of semiconducting p-type diamond thin film electrodes, *J. Electrochem. Soc.* **144**, L142 (1997).
- [29] Y. V. Pleskov, V. M. Mazin, Y. E. Evstefeeva, V. P. Varnin, I. G. Teremetskaya, and V. A. Laptev, Photoelectrochemical determination of the flatband potential of boron-doped diamond, *Electrochem. Solid-State Lett.* **3**, 141 (2000).
- [30] A. Chambers, S. Prawer, A. Ahnood, and H. Zhan, Diamond supercapacitors: Towards durable, safe, and biocompatible aqueous-based energy storage, *Front. Chem.* **10**, 924127 (2022).
- [31] A. Chambers, A. Ahnood, S. Falahatdoost, S. Yianni, D. Hoxley, B. C. Johnson, D. J. Garrett, S. Tomljenovic-Hanic, and S. Prawer, Near-infrared excitation of nitrogen-doped ultrananocrystalline diamond photoelectrodes in saline solution, *Diamond Relat. Mater.* **103**, 107720 (2020).
- [32] A. Ahnood, A. N. Simonov, J. S. Laird, M. I. Maturana, K. Ganesan, A. Stacey, M. R. Ibbotson, L. Spiccia, and S. Prawer, Transient photoresponse of nitrogen-doped ultrananocrystalline diamond electrodes in saline solution, *Appl. Phys. Lett.* **108**, 104103 (2016).
- [33] S. Falahatdoost, A. Chambers, A. Stacey, H. N. Al Hashem, A. Nadarajah, S. Prawer, and A. Ahnood, Enhanced electrochemical capacitance of nitrogen-doped ultrananocrystalline diamond through oxygen treatment, *Appl. Surf. Sci.* **543**, 148768 (2021).
- [34] J. Raymakers, K. Haenen, and W. Maes, Diamond surface functionalization: from gemstone to photoelectrochemical applications, *J. Mater. Chem. C* **7**, 10134 (2019).
- [35] Z. Jian, N. Yang, M. Vogel, Z. Zhou, G. Zhao, P. Kienitz, A. Schulte, H. Schönherr, T. Jiao, W. Zhang, and X. Jiang, Tunable photo-electrochemistry of patterned TiO<sub>2</sub>/BDD heterojunctions, *Small Methods* **4** (9), 2000257 (2020).
- [36] See Supplemental Material at <http://link.aps.org/supplemental/10.1103/zhcb-13pn> in which Refs. [22,24,37–42] are cited, for additional information about x-ray absorption spectroscopy.
- [37] E. M. Zagrebina, A. V. Generalov, A. Y. Klyushin, K. A. Simonov, N. A. Vinogradov, M. Dubois, L. Frezet, N. Mårtensson, A. B. Preobrajenski, and A. S. Vinogradov, Comparative NEXAFS, NMR, and FTIR study of various-sized nanodiamonds: as-prepared and fluorinated, *J. Phys. Chem. C* **119**, 835 (2015).
- [38] J. F. Morar, F. J. Himpsel, G. Hollinger, J. L. Jordon, G. Hughes, and F. R. McFeely, C 1s excitation studies of diamond (111). II. Unoccupied surface states, *Phys. Rev. B* **33**, 1346 (1986).
- [39] A. Laikhtman, I. Gouzman, A. Hoffman, G. Comtet, L. Hellner, and G. Dujardin, Sensitivity of near-edge x-ray absorption fine structure spectroscopy to ion beam damage in diamond films, *J. Appl. Phys.* **86**, 4192 (1999).
- [40] A. Laikhtman and A. Hoffman, Interaction of thermally activated and molecular oxygen with hydrogenated polycrystalline diamond surfaces studied by synchrotron radiation techniques, *Surf. Sci. Lett.* **522**, L1 (2003).
- [41] A. Hoffman, G. Comtet, L. Hellner, G. Dujardin, and M. Petracic, Surface near-edge x-ray adsorption fine structure of hydrogenated diamond films and Di(100) surfaces studied by H<sup>+</sup> and H<sup>-</sup> ion desorption, *Appl. Phys. Lett.* **73**, 1152 (1998).
- [42] E. F. Aziz, J. Xiao, R. Golnak, and M. Tesch, LiXEdrom: High energy resolution RIXS station dedicated to liquid investigation at BESSY II, *J. Large-Scale Res. Facil.* **2**, A80 (2016).
- [43] M. Mastellone, A. Bellucci, M. Girolami, V. Serpente, R. Polini, S. Orlando, A. Santagata, E. Sani, F. Hitzel, and D. M. Trucchi, Deep-subwavelength 2D periodic surface nanostructures on diamond by double-pulse femtosecond laser irradiation, *Nano Lett.* **21**, 4477 (2021).
- [44] A. F. Sartori, S. Orlando, A. Bellucci, D. M. Trucchi, S. Abrahami, T. Boehme, T. Hantschel, W. Vandervorst, and J. G. Buijnsters, Laser-induced periodic surface structures (LIPSS) on heavily boron-doped diamond for electrode applications, *ACS Appl. Mater. Interfaces* **10**, 43236 (2018).
- [45] M. Girolami, A. Bellucci, M. Mastellone, S. Orlando, V. Serpente, V. Valentini, R. Polini, E. Sani, T. De Caro, and D. M. Trucchi, Femtosecond-laser nanostructuring of black diamond films under different gas environments, *Materials* **13**, 1 (2020).
- [46] See Supplemental Material at <http://link.aps.org/supplemental/10.1103/zhcb-13pn> for additional information about the CV characterization.
- [47] F. Maier, J. Ristein, and L. Ley, Electron affinity of plasma-hydrogenated and chemically oxidized diamond (100) surfaces, *Phys. Rev. B* **64**, 165411 (2001).
- [48] D. Miliáieva, A. S. Djoumessi, J. Čermák, K. Kolářová, M. Schaal, F. Otto, E. Shagieva, O. Romanyuk, J. Pangrác, J. Kuliček, V. Nádaždy, Š. Stehlík, A. Kromka, H. Hoppe, and B. Rezek, Absolute energy levels in nanodiamonds of different origins and surface chemistries, *Nanoscale Adv.* **5**, 4402 (2023).
- [49] V. S. Srikanth, P. S. Kumar, and V. B. Kumar, A Brief Review on the In Situ Synthesis of Boron-Doped Diamond Thin Films, *Int. J. Electrochem.* **1**, 2090 (2012).

- [50] See Supplemental Material at <http://link.aps.org/supplemental/10.1103/zhcb-13pn> in which Ref. [51] is cited, for additional information about the surface band bending and double-layer potential drop.
- [51] R. Van de Krol and M. Grätzel, in *Photoelectrochemical Hydrogen Production*, edited by R. van de Krol and M. Grätzel (Springer, New York, 2012), Vol. 90, pp. 15.
- [52] V. Chakrapani, J. C. Angus, A. B. Anderson, S. D. Wolter, B. R. Stoner, and G. U. Sumanasekera, Charge transfer equilibria between diamond and an aqueous oxygen electrochemical redox couple, *Science* **318**, 1424 (2007).
- [53] M. V. Hauf, P. Simon, M. Seifert, A. W. Holleitner, M. Stutzmann, and J. A. Garrido, Low dimensionality of the surface conductivity of diamond, *Phys. Rev. B* **89** (11), 115426 (2014).
- [54] J. A. Garrido, A. Härtl, M. Dankerl, A. Reitingner, M. Eickhoff, A. Helwig, G. Müller, and M. Stutzmann, The surface conductivity at the diamond/aqueous electrolyte interface, *J. Am. Chem. Soc.* **130**, 4177 (2008).
- [55] A. Härtl, J. A. Garrido, S. Nowy, R. Zimmermann, C. Werner, D. Horinek, R. Netz, and M. Stutzmann, The ion sensitivity of surface conductive single crystalline diamond, *J. Am. Chem. Soc.* **129**, 1287 (2007).
- [56] S. R. Morrison, *Electrochemistry at Semiconductor and Oxidized Metal Electrodes* (Springer, New York, NY, 1980).
- [57] See Supplemental Material at <http://link.aps.org/supplemental/10.1103/zhcb-13pn> in which Ref. [48] is cited, for additional information about the determination of the Fermi level from  $E_{WE}$ .
- [58] M. Rusu, T. Kodalle, L. Choubrac, N. Barreau, C. A. Kaufmann, R. Schlattmann, and T. Unold, Electronic structure of the CdS/Cu(In,Ga)Se<sub>2</sub> interface of KF- and RbF-treated samples by Kelvin probe and photoelectron yield spectroscopy, *ACS Appl. Mater. Interfaces* **13**, 7745 (2021).
- [59] See Supplemental Material at <http://link.aps.org/supplemental/10.1103/zhcb-13pn> in which Refs. [24,58,60,61] are cited, for additional information about photoelectron yield spectroscopy.
- [60] K. C. Prince, R. Richter, M. De Simone, M. Alagia, and M. Coreno, Near edge X-ray absorption spectra of some small polyatomic molecules, *J. Phys. Chem. A* **107**, 1955 (2003).
- [61] H. Shinotsuka, S. Tanuma, C. J. Powell, and D. R. Penn, Calculations of electron inelastic mean free paths. X. Data for 41 elemental solids over the 50 eV to 200 keV range with the relativistic full Penn algorithm, *Surf. Interface Anal.* **47**, 871 (2015).
- [62] A. Chemin, M. K. Kuntumalla, M. Brzhezinskaya, T. Petit, and A. Hoffman, Depth profiling of microwave nitrogen-terminated polycrystalline diamond surfaces by energy-dependent X-ray photoelectron spectroscopy, *Appl. Surf. Sci.* **661**, 160082 (2024).
- [63] R. Malkinson, M. K. Kuntumalla, A. Hoffman, and N. Bar-Gill, Enhanced quantum properties of shallow diamond atomic defects through nitrogen surface termination, *J. Mater. Chem. C* **12**, 7206 (2023).
- [64] J. B. Cui, J. Ristein, and L. Ley, Low-threshold electron emission from diamond, *Phys. Rev. B* **60**, 16135 (1999).
- [65] F. Ducrozet, E. Brun, H. A. Girard, J. C. Arnault, and C. Sicard-Roselli, Milled nanodiamonds overproduce solvated electrons while scavenging hydroxyl radicals under gamma irradiation, *J. Phys. Chem. C* **127**, 19544 (2023).
- [66] See Supplemental Material at <http://link.aps.org/supplemental/10.1103/zhcb-13pn> for additional information about the solvated electron dosing.
- [67] A. Hankin, F. E. Bedoya-Lora, J. C. Alexander, A. Regoutz, and G. H. Kelsall, Flat band potential determination: avoiding the pitfalls, *J. Mater. Chem. A* **7**, 26162 (2019).
- [68] K. Xu, D. Pagliero, G. I. López-Morales, J. Flick, A. Wolcott, and C. A. Meriles, Photoinduced charge injection from shallow point defects in diamond into water, *ACS Appl. Mater. Interfaces* **16**, 37226 (2024).
- [69] S. Falahatdoost, A. Chambers, A. Stacey, S. Praver, and A. Ahnood, Towards optical neuromodulation using nitrogen-doped ultrananocrystalline diamond photoelectrodes, *Surf. Interfaces* **30**, 101850 (2022).
- [70] A. Chambers, S. Praver, and A. Ahnood, Photoelectrochemical Modelling of Semiconducting Electrodes for Neural Interfacing, *J. Electrochem. Soc.* **170**, 026502 (2023).
- [71] See Supplemental Material at <http://link.aps.org/supplemental/10.1103/zhcb-13pn> for additional information about the photocurrent power dependency.
- [72] See Supplemental Material at <http://link.aps.org/supplemental/10.1103/zhcb-13pn> in which Ref. [24] is cited, for additional information about the photocurrent fit.
- [73] S. Ferro, M. Dal Colle, and A. De Battisti, Chemical surface characterization of electrochemically and thermally oxidized boron-doped diamond film electrodes, *Carbon* **43**, 1191 (2005).
- [74] C. D. Clark, P. J. Dean, and P. V. Harris, Intrinsic edge absorption in diamond, *Proc. R. Soc. London, Ser. A* **277**, 312 (1964).
- [75] Dittrich Thomas, Transient surface photovoltage spectroscopy of diamond, *AIP Adv.* **12**, 065206 (2022).
- [76] T. Dittrich and S. Fengler, Transitions in polycrystalline diamond probed by steady state, modulated and transient surface photovoltage spectroscopy, *Semicond. Sci. Technol.* **38**, 015015 (2023).
- [77] T. Petit, M. Lounasvuori, A. Chemin, and P. Bärmann, Nanointerfaces: Concepts and strategies for optical and X-ray spectroscopic characterization, *ACS Phys. Chem. Au* **3** (3), 263 (2023).
- [78] See Supplemental Material at <http://link.aps.org/supplemental/10.1103/zhcb-13pn> for additional information about the photocurrent cyclic voltammetry.
- [79] Y. Cai, A. B. Anderson, J. C. Angus, and L. N. Kostadinov, Hydrogen evolution on diamond electrodes by the Volmer-Heyrovsky mechanism: Prediction of reversible potentials and activation energies, *J. Electrochem. Soc.* **154** (2), F36 (2006).
- [80] H. Ooka, M. E. Wintzer, and R. Nakamura, Non-zero binding enhances kinetics of catalysis: Machine learning analysis on the experimental hydrogen binding energy of platinum, *ACS Catal.* **11** (10), 6298 (2021).